Reducing Parametric Uncertainty in Limit Cycle Oscillations

R. Hayes[1][*] , R. Dwight[2][†] and S. Marques[1][‡]

[1] *Queen's University Belfast, Belfast, BT9 5AH, United Kingdom*

[2] *Delft University of Technology, 2629 HS Delft, Netherlands*

3rd ECCOMAS Young Investigators Conference (YIC)

The assimilation of discrete higher fidelity data points with model predictions can be used to achieve a reduction in the uncertainty of the model input parameters which generate accurate predictions. The problem investigated here involves the prediction of limit-cycle oscillations using a High-Dimensional Harmonic Balance method (HDHB). The efficiency of the HDHB method is exploited to enable calibration of structural input parameters using a Bayesian inference technique. Markov-chain Monte Carlo is employed to sample the posterior distributions. Parameter estimation is carried out on both a pitch/plunge aerofoil and Goland wing configuration. In both cases significant refinement was achieved in the distribution of possible structural parameters allowing better predictions of their true deterministic values.

I.   Introduction

As simulation tools are created for problems of higher complexity, it becomes increasingly difficult for practitioners to be confident that their model accurately replicates the physical behaviour of the phenomena of interest. Furthermore, if an adequate physical description of the system is implemented, ensuring all parameters and coefficients which drive the simulation are accurately defined can be problematic. This adversely affects the calibration and validation processes during the development of the simulation tool. Various dynamic aeroelastic phenomena provide good examples of complex physical behaviour which are dependent on many parameters that are rife with variability and are difficult to ascertain. Due to the highly variable nature of both the structural and flow characteristics, Pettit has identified the need for consideration of parametric uncertainty in the prediction of aeroelastic stability.[1] This uncertainty is epistemic in nature and arises from lack of understanding about subtle characteristics of the structural body and local flow conditions. Subsequently, much research has been carried out to investigate how parametric uncertainty influences the aeroelastic behaviour of the aircraft.

Marques *et al* investigated the impact of structural variability on transonic flutter predictions for a range of models and illustrated the high sensitivity of aeroelastic stability.[2,3] Limit cycle oscillations (LCO) are a different aeroelastic phenomenon and is a pertinent issue for some *in-service* aircraft due to their nonlinear nature, hence they carry considerable practical interest.[4,5] As for flutter, LCOs are sensitive to parametric variability and have been investigated using various uncertainty propagation techniques.[6–9] Despite the many studies conducted to examine the consequences of parametric uncertainty there have been few attempts to characterise this uncertainty for aeroelastic problems. By using experimental data, e.g. from flight tests, to accurately calibrate models, stochastic analysis of aeroelastic phenomena can be carried out using more sophisticated uncertainty propagation tools with a high degree of confidence.

Bayesian inference is a technique tailored for using external evidence to reduce the epistemic uncertainty in the problem. The Bayesian framework is applicable to the calibration of models and identification of input parameters.[10] It has been applied to structural variability and CFD problems with promising results.[11,12] Dwight *et al* reduced uncertainty in the predictions of flutter speeds based on epistemic variability on

---

[*]PhD student, QUB, rhayes04@qub.ac.uk

[†]Lecturer, TU Delft, r.p.dwight@tudelft.nl

[‡]Lecturer, QUB, s.marques@qub.ac.uk

numerous structural parameters.[13] The work presented in this paper focuses on implementing a Bayesian inference strategy driven by a Markov-chain Monte Carlo (MCMC) algorithm to estimate model parameters which ultimately will improve model performance. First, an HDHB formulation is exploited to determine the LCO conditions without incurring the high costs of time-accurate simulations; then the practicality of using the HDHB approach to drive the MCMC algorithm for the parameter estimation is investigated. The paper will first summarize the HDHB formulation, followed by a description of the Bayesian inference strategy and source of *experimental* data. Finally, results from the model calibration are presented and discussed.

II.   High Dimensional Harmonic Balance

The HDHB formulation used in this work was proposed by Hall *et al*[14] for time-periodic flow problems, this methodology was adapted to nonlinear dynamical systems by Liu *et al*[15] and is summarised next. Consider a dynamic system with a nonlinearity in stiffness whose behaviour can be described using a simple equation of motion given by:

$$\mathbf{M}\ddot{x} + \mathbf{C}\dot{x} + \mathbf{K}x + \mathbf{K}_{nl}(x) = \mathbf{F}(x, \dot{x}, \ddot{x}, t) \tag{1}$$

Matrices $\mathbf{M}$, $\mathbf{C}$ and $\mathbf{K}$ describe the mass, damping and linear stiffness properties of the system respectively and $\mathbf{K}_{nl}(x)$ is the nonlinear component of the stiffness restoring force. The external force, $\mathbf{F}$ can be a function of the motion of the system and time. Here, consider the external force to be, $\mathbf{F} = \sin(\omega t)$. The solution of eq. (1) can be approximated to be a truncated Fourier series of N_H harmonics with a fundamental frequency denoted by ω.

$$x(t) \approx \hat{x}_0 + \sum_{n=1}^{N_H}(\hat{x}_{2n-1}\cos(n\omega t) + \hat{x}_{2n}\sin(n\omega t)) \tag{2}$$

The first and second derivatives of $x(t)$ with respect to time can be found to be:

$$\dot{x}(t) \approx \sum_{n=1}^{N_H}(-n\omega\hat{x}_{2n-1}\sin(n\omega t) + n\omega\hat{x}_{2n}\cos(n\omega t)) \tag{3}$$

$$\ddot{x}(t) \approx \sum_{n=1}^{N_H}(-(n\omega)^2\hat{x}_{2n-1}\cos(n\omega t) - (n\omega)^2\hat{x}_{2n}\sin(n\omega t)) \tag{4}$$

By substituting the Fourier series back into eq. (1) and collecting terms associated with each harmonic, a system of equations can be assembled that relate the system's dynamic properties with the Fourier coefficients. This algebraic system consists of $2N_H+1$ equations which can be conveniently displayed in vector form:

$$(\mathbf{M}\omega^2\mathbf{A}^2 + \mathbf{C}\omega\mathbf{A} + \mathbf{KI})\hat{\mathbf{Q}} + \hat{\mathbf{Q}}_{nl} - \mathbf{F}\hat{\mathbf{H}} = 0 \tag{5}$$

where:

$$\hat{\mathbf{Q}} = \left\{\begin{array}{c}\hat{x}_0 \\ \hat{x}_1 \\ \hat{x}_2 \\ \hat{x}_3 \\ \vdots \\ \hat{x}_{2N_H}\end{array}\right\}_{2N_H+1}, \quad \hat{\mathbf{Q}}_{nl} = \left\{\begin{array}{c}\hat{K_{nl0}} \\ \hat{K_{nl1}} \\ \hat{K_{nl2}} \\ \hat{K_{nl3}} \\ \vdots \\ \hat{K_{nl2N_H}}\end{array}\right\}_{2N_H+1} \quad \text{and } \hat{\mathbf{H}} = \left\{\begin{array}{c}0 \\ 0 \\ 1 \\ 0 \\ \vdots \\ 0\end{array}\right\}_{2N_H+1}$$

Matrix $\mathbf{A}$ reconstructs the Fourier series from the harmonic balancing and is shown in.[9] The nonlinear term Fourier coefficients, $\hat{\mathbf{Q}}_{nl}$ are computed using discrete Fourier transforms (DFT). Computing these terms analytically can be cumbersome for certain types of nonlinearities such as high order polynomial terms or fluxes in CFD problems.[14] The HDHB method overcomes these issues by casting the problem in the time domain where the Fourier coefficients are related to $2N_H + 1$ equally spaced sub-time levels throughout one temporal period using a constant transformation matrix which yields:

$$\hat{\mathbf{Q}} = \mathbf{E}\tilde{\mathbf{Q}}, \ \hat{\mathbf{Q}}_{nl} = \mathbf{E}\tilde{\mathbf{Q}}_{nl} \ \text{ and } \ \hat{\mathbf{H}} = \mathbf{E}\tilde{\mathbf{H}} \tag{6}$$

where:

$$
\tilde{\mathbf{Q}} = \left\{ \begin{array}{c} x(t_0) \\ x(t_1) \\ \vdots \\ x(t_{2N_H}) \end{array} \right\}, \quad \tilde{\mathbf{Q}}_{nl} = \left\{ \begin{array}{c} K_{nl}(x(t_0)) \\ K_{nl}(x(t_1)) \\ \vdots \\ K_{nl}(x(t_{2N_H})) \end{array} \right\} \text{ and } \tilde{\mathbf{H}} = \left\{ \begin{array}{c} \sin t_0 \\ \sin t_1 \\ \vdots \\ \sin t_{2N_H} \end{array} \right\}
$$

and

$$
t_i = \frac{i2\pi}{2N_H + 1}(i = 0, 1, ..., 2N_H) \tag{7}
$$

Expressions for the transformation matrix, $\mathbf{E}$ and its inverse, $\mathbf{E}^{-1}$ which can be used to relate the time domain variables back to the Fourier coefficients ie. $\tilde{\mathbf{Q}} = \mathbf{E}^{-1}\hat{\mathbf{Q}}$ are shown in.[9] Using these transformation matrices, the system in eq. (5) can be cast in the time domain as:

$$
(\mathbf{M}\omega^2\mathbf{D}^2 + \mathbf{C}\omega\mathbf{D} + \mathbf{KI})\tilde{\mathbf{Q}} + \tilde{\mathbf{Q}}_{nl} - \mathbf{F}\tilde{\mathbf{H}} = 0 = \mathbf{R} \tag{8}
$$

where $\mathbf{D} = \mathbf{E}^{-1}\mathbf{AE}$. Equation (8) represents the HDHB system and can be solved using either pseudo-time marching or Newton-Raphson approaches. Here, the latter is employed:

$$
\mathbf{S}^{n+1} = \mathbf{S}^n - \lambda\mathbf{J}^{-1}\mathbf{R}^n \tag{9}
$$

where $\mathbf{S}^n$ is the solution vector at iteration n, λ is a relaxation parameter for increased stability. The inverse Jacobian of the system, $\mathbf{J}^{-1}$, is numerically approximated using finite-differences[16] and $\mathbf{R}^n$ is the residual of eq. (8) at iteration n, ie.

$$
\mathbf{S}^n = \left\{ \begin{array}{c} \hat{x}_0 \\ \hat{x}_1 \\ \vdots \\ \hat{x}_{2N_H} \end{array} \right\}^n, \quad \mathbf{R}^n = \left\{ \begin{array}{c} R_0 \\ R_1 \\ \vdots \\ R_{2N_H} \end{array} \right\}^n \text{ and } \mathbf{J} = \left[\begin{array}{ccc} \frac{\partial R_0}{\partial \hat{x}_0} & \cdots & \frac{\partial R_0}{\partial \hat{x}_{2N_H}} \\ \vdots & \ddots & \vdots \\ \frac{\partial R_{2N_H}}{\partial \hat{x}_0} & \cdots & \frac{\partial R_{2N_H}}{\partial \hat{x}_{2N_H}} \end{array} \right]
$$

III. Bayesian Inference

Bayesian inference updates the probability that the model matches real data based on discrete pieces of evidence and uses Bayes' rule to compute the posterior probability distributions:

$$
P(m|d) \propto P(d|m)P_0(m) \tag{10}
$$

where $P_0(m)$ is the prior which describes the *perceived* probability of the model generating accurate predictions before any evidence is observed. The likelihood, $P(d|m)$, measures the probability of observing evidence, d given the model output, m. The posterior is given as $P(m|d)$. This is the probability that the model can replicate real data based on the evidence observed.

For the uncertainties of the input parameters to be updated, first the model needs to be related to the data using a statistical model. In this work, the statistical model described by Kennedy and O'Hagan[10] is employed:

$$
d = m(\theta) + \epsilon(0, \sigma_\epsilon) \tag{11}
$$

where $m(\theta)$ is the model output for a particular set of input parameters, θ. This statistical model represents the error between the model and experimental data as noise, ϵ which is described by a normal distribution with mean 0 and standard deviation σ_ϵ. By maximising the posterior probability, a deterministic value of θ can be found which gives the most accurate model predictions based on the observed evidence. To achieve this Markov-Chain Monte Carlo is used and is described below.

Markov-Chain Monte Carlo

Markov-Chain Monte Carlo (MCMC) is a *random walk* method used to sample a probability space and find the desired probability distribution. For the statistical model in this work the likelihood is expressed as:

$$
P(d|m)^n = exp\left(-\frac{1}{2} \sum_{i=1}^{k} \frac{(d(i) - m(i, \theta))^2}{\sigma_\epsilon^2} \right) \tag{12}
$$

The posterior is used to drive the MCMC and the criteria for accepting samples is given as:

$$\begin{cases} \dfrac{P(m|d)^n}{P(m|d)^{n-1}} \geq 1, \text{ accept with probability of } 1 \\[3mm] \dfrac{P(m|d)^n}{P(m|d)^{n-1}} < 1, \text{ accept with probability of } \dfrac{P(m|d)^n}{P(m|d)^{n-1}} \\[3mm] \dfrac{P(m|d)^n}{P(m|d)^{n-1}} < 1, \text{ reject with probability of } 1 - \dfrac{P(m|d)^n}{P(m|d)^{n-1}} \end{cases} \tag{13}$$

This algorithm is known as the Metropolis-Hastings algorithm[17] and is a commonly used form of Markov Chain methods. If sufficient MCMC samples are used and an initial burn-in phase is removed, a statistically accurate distribution of the posterior can be found.

IV. Pitch-Plunge Aerofoil

The equations of motion for a pitch/plunge aerofoil with nonlinear restoring forces are shown in reference.[18] They can be displayed in the form of eq. (1) where the terms are given as:

$$\mathbf{M} = \begin{bmatrix} x_\alpha & 1 \\ 1 & \dfrac{x_\alpha}{r_\alpha^2} \end{bmatrix}, \quad \mathbf{C} = \begin{bmatrix} 0 & \dfrac{2\zeta_\xi \overline{\omega}}{V^*} \\ \dfrac{2\zeta_\alpha}{V^*}\dot{\alpha} & 0 \end{bmatrix}, \quad \mathbf{K} = \begin{bmatrix} 0 & \dfrac{k_\xi \overline{\omega}^2}{V^{*2}} \\ \dfrac{k_\alpha}{V^{*2}} & 0 \end{bmatrix},$$

$$x = \begin{Bmatrix} \alpha \\ \xi \end{Bmatrix}, \quad \mathbf{K}_{nl} = \begin{bmatrix} 0 & \dfrac{\beta_\xi \overline{\omega}^2}{V^{*2}} \\ \dfrac{\beta_\alpha}{V^{*2}} & 0 \end{bmatrix} \begin{Bmatrix} \alpha^3 \\ \xi^3 \end{Bmatrix}, \quad \mathbf{F} = \begin{Bmatrix} -\dfrac{C_L(\tau)}{\pi\mu} + \dfrac{bP(\tau)}{mV^2} \\ \dfrac{2C_M(\tau)}{\pi\mu r_\alpha^2} + \dfrac{Q(\tau)}{mV^2 r_\alpha^2} \end{Bmatrix}$$

The non-dimensional plunge displacement of the elastic axis is given by ξ and α represents the pitch. C_L and C_m correspond to the lift and pitching moment coefficients, $P(\tau)$ and $Q(\tau)$ denote external forces and moments respectively. After the introduction of four new variables, w_1, w_2, w_3, w_4 which partially describe the aerodynamic and external forces characterised by $\mathbf{F}$, the equations of motion and generalised aerodynamic terms can be written as:

$$\begin{cases} c_0\xi'' + c_1\alpha'' + c_2\xi' + c_3\alpha' + c_4\xi + c_{5_\beta}\xi^3 + c_6\alpha + c_7w_1 + c_8w_2 + c_9w_3 + c_{10}w_4 = f(t^*) \\ d_0\xi'' + d_1\alpha'' + d_2\alpha' + d_3\alpha + d_{4_\beta}\alpha^3 + d_5\xi' + d_6\xi + d_7w_1 + d_8w_2 + d_9w_3 + d_{10}w_4 = g(t^*) \\ w_1' = \alpha - \epsilon_1 w_1 \\ w_2' = \alpha - \epsilon_2 w_2 \\ w_3' = \alpha - \epsilon_1 w_3 \\ w_4' = \alpha - \epsilon_2 w_4 \end{cases} \tag{14}$$

where $f(t^*)$ and $g(t^*)$ represent the transient component of the generalised aerodynamic forces and damp out with time hence are not part of the periodic solution. Expressions for the coefficients of system (14) can be found in.[19] Implementing the HDHB approach to system (14) yields a system in the frequency domain.

$$\begin{cases} (c_0\omega^2\mathbf{A}^2 + c_2\omega\mathbf{A} + c_4\mathbf{I})\hat{\mathbf{Q}}_\xi + (c_1\omega^2\mathbf{A}^2 + c_3\omega\mathbf{A} + c_6\mathbf{I})\hat{\mathbf{Q}}_\alpha + \sum_{i=1}^4 c_{6+i}\hat{\mathbf{Q}}_{w_i} = 0 \\ (d_0\omega^2\mathbf{A}^2 + d_5\omega\mathbf{A} + d_6\mathbf{I})\hat{\mathbf{Q}}_\xi + (d_1\omega^2\mathbf{A}^2 + d_2\omega\mathbf{A} + d_3\mathbf{I})\hat{\mathbf{Q}}_\alpha + \sum_{i=1}^4 d_{6+i}\hat{\mathbf{Q}}_{w_i} + d_{4_\beta}\hat{\mathbf{Q}}_{\beta_\alpha} = 0 \\ (\omega\mathbf{A} + \epsilon_1\mathbf{I})\hat{\mathbf{Q}}_{w_1} - \hat{\mathbf{Q}}_\alpha = 0 \\ (\omega\mathbf{A} + \epsilon_2\mathbf{I})\hat{\mathbf{Q}}_{w_2} - \hat{\mathbf{Q}}_\alpha = 0 \\ (\omega\mathbf{A} + \epsilon_1\mathbf{I})\hat{\mathbf{Q}}_{w_3} - \hat{\mathbf{Q}}_\xi = 0 \\ (\omega\mathbf{A} + \epsilon_2\mathbf{I})\hat{\mathbf{Q}}_{w_4} - \hat{\mathbf{Q}}_\xi = 0 \end{cases} \tag{15}$$

By substituting the last 4 equations of system (15) into the first 2 and replacing $\hat{\mathbf{Q}}_{\beta_\alpha}$ with $\mathbf{E}(\mathbf{E}^{-1}\hat{\mathbf{Q}}_\alpha)^3$ the system can be further reduced to:[15]

$$(\mathbf{A}_2 - \mathbf{B}_2\mathbf{B}_1^{-1}\mathbf{A}_1)\hat{\mathbf{Q}}_\alpha + d_{4_\beta}\mathbf{E}(\mathbf{E}^{-1}\hat{\mathbf{Q}}_\alpha)^3 = 0 \tag{16}$$

where the matrices $\mathbf{A}_\bullet$ and $\mathbf{B}_\bullet$ are given by:

$$\begin{aligned}
\mathbf{A}_1 &= c_1\omega^2\mathbf{A}^2 + c_3\omega\mathbf{A} + c_6\mathbf{I} + c_8(\omega\mathbf{A} + \epsilon_1\mathbf{I})^{-1} + c_9(\omega\mathbf{A} + \epsilon_2\mathbf{I})^{-1} \tag{17} \\
\mathbf{B}_1 &= c_0\omega^2\mathbf{A}^2 + c_2\omega\mathbf{A} + c_4\mathbf{I} + c_{10}(\omega\mathbf{A} + \epsilon_1\mathbf{I})^{-1} + c_{11}(\omega\mathbf{A} + \epsilon_2\mathbf{I})^{-1} \tag{18} \\
\mathbf{A}_2 &= d_1\omega^2\mathbf{A}^2 + d_2\omega\mathbf{A} + d_3\mathbf{I} + d_7(\omega\mathbf{A} + \epsilon_1\mathbf{I})^{-1} + d_8(\omega\mathbf{A} + \epsilon_2\mathbf{I})^{-1} \tag{19} \\
\mathbf{B}_2 &= d_0\omega^2\mathbf{A}^2 + d_5\omega\mathbf{A} + d_6\mathbf{I} + d_9(\omega\mathbf{A} + \epsilon_1\mathbf{I})^{-1} + d_{10}(\omega\mathbf{A} + \epsilon_2\mathbf{I})^{-1} \tag{20}
\end{aligned}$$

Equation (16) represents the HDHB system which will be solved in our model. The frequency of the response is not constrained in this type of problem, hence it must be treated as a variable in conjunction with the amplitude properties in order to capture the behaviour of the system. This is achieved by setting $\hat{\alpha}_1 = 0$ and including ω in the solution vector which will create a system of $2N_H + 1$ equations with $2N_H + 1$ unknowns and affect only the phase of the solution. The frequency can then be simultaneously solved along with the Fourier coefficients using the Newton-Raphson scheme. The solution and residual vectors are now given by:

$$\mathbf{S}^n = \left\{\begin{array}{c} \omega \\ \hat{\alpha}_0 \\ \hat{\alpha}_2 \\ \vdots \\ \hat{\alpha}_{2N_H} \end{array}\right\}^n , \quad \mathbf{R}^n = \left\{\begin{array}{c} R_1 \\ R_0 \\ R_2 \\ \vdots \\ R_{2N_H} \end{array}\right\}^n$$

Results

The system parameters used for this case are $\bar{\omega} = 0.2$, $\mu = 100$, $a_h = 0.5$, $x_\alpha = 0.25$, $r_\alpha = 0.5$ and $\zeta_\xi = 0$. The MCMC algorithm is run using 20000 samples with a burn-in phase of 1000 samples. The uncertain parameters are the cubic stiffness coefficient, β_α and the damping ratio, ζ_α of the aerofoil and have *true* values of 4 and 0.25 respectively.
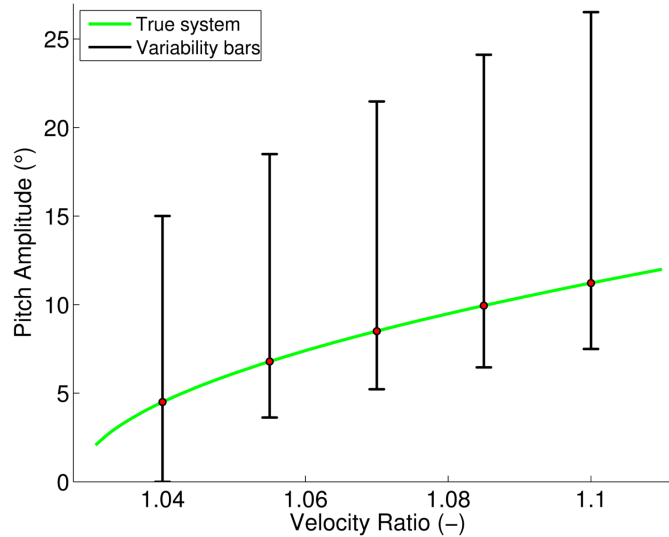

Figure 1. Uncertainty bars of aerofoil for variability across entire parameter space

The MCMC will search the parameter space for values of these parameters which best allow the HDHB to replicate the *experimental* data where the HDHB is computed using 1 harmonic. The experimental data is in fact LCO amplitudes which are simulated using our model but we assume we do not know the true

parameter values *a priori*. The different data points are computed with the model using these true values but at different velocities yielding different values of amplitude. We assume we know the values of velocity from which each data point originates.

When no experimental data is available, our prior knowledge of the system is the only resource for predicting suitable values for these parameters. Here, the probability of a parameter taking any value within its possible range is assumed to be equal so uniform distributions are assigned to each variable hence the initial distribution is the entire parameter space. This represents an uninformative prior and has no influence on the shape of the posterior distribution. As the true values of the parameters are not known, the parameter space covers a wide range to ensure that it contains the true values. The space ranges from 1 to 7 for cubic stiffness and 0 to 0.5 for damping ratio. The variability of LCO amplitude contained within the parameter space is shown in Figure 1 and as expected a significant amount of variability is present.

Figure 2 shows the posterior distribution and parameter distributions computed by the Bayesian inference when one experimental data point at a velocity ratio of 1.07 is included. The colouring of the posterior in Figure 3(a) depicts the probability that the model performs correctly, the red representing high probability and the blue representing low probability. The white regions indicate zero probability that the model can replicate the experimental data. The histograms in Figure 2(b) show the influence of one data point on each parameter individually; a reduction of 35.6% in the range of cubic stiffness is observed while only a reduction of 3.4% is exhibited for damping ratio. It is important to note that the parameter histograms alone do not illustrate the extent of the reduction in variability because the histograms do not provide any information on the shape of the posterior. Solely from the histograms it can be inferred that the true value lies within a rectangular region which is 37.9% smaller than the prior parameter space. Immediately from examining the colour plot in Figure 3(a) it is obvious that a much greater reduction has occurred, approximately 94.2%. This is due to the slender profile of the posterior which is caused by the direct influence of each parameter on LCO amplitude; as one parameter changes, the other must change to allow the model to perform well.

(a) Posterior Distribution

(b) θ histograms
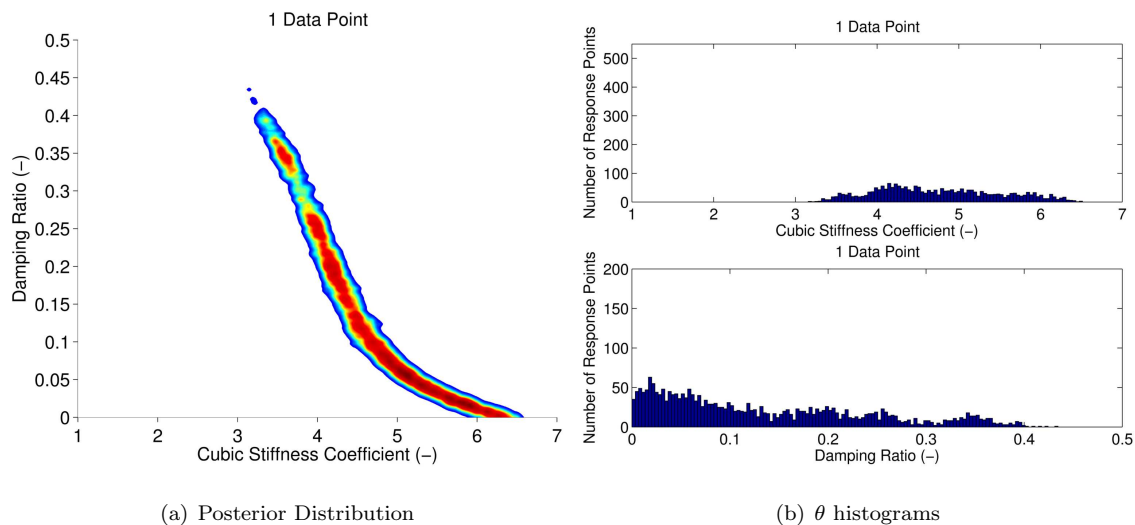
Figure 2. Posterior and parameter distributions using data from 1 velocity - Aerofoil

After including two experimental points at the velocities 1.07 and 1.1, another clear reduction in the spread of the two variables is shown in Figure 3. The spread of the cubic stiffness coefficient is less than that of the damping ratio which suggests that the system is more sensitive to the cubic stiffness. The addition of another point, at a velocity of 1.04, yields another refinement of the posterior distribution as shown in Figure 4. The posterior for 5 data points at velocities $[1.04, 1.055, 1.07, 1.85, 1.1]$ is shown in Figure 5(a). The histograms in Figure 5(b) show well defined probability distributions which are approximately Gaussian. From Table 1 it is clear that the introduction of new experimental evidence enable the posterior distributions to converge to the true values, providing the evidence is not contradictory. Not only do the mean values converge to the true values, the standard deviation of the parameter distributions decrease with increasing amounts of evidence. From the distributions in this case, predictions of the true parameter values would be fairly accurate. By refining posterior distributions, model calibrations can be carried out to enable more accurate predictions of the problem of interest.
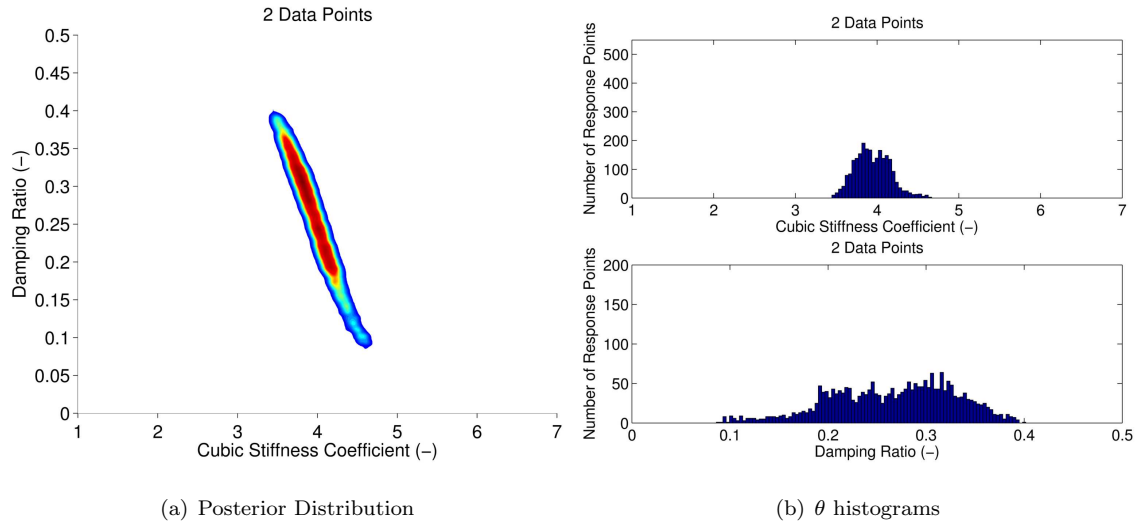
(a) Posterior Distribution

(b) θ histograms

Figure 3. Posterior and parameter distributions using data from 2 velocities - Aerofoil
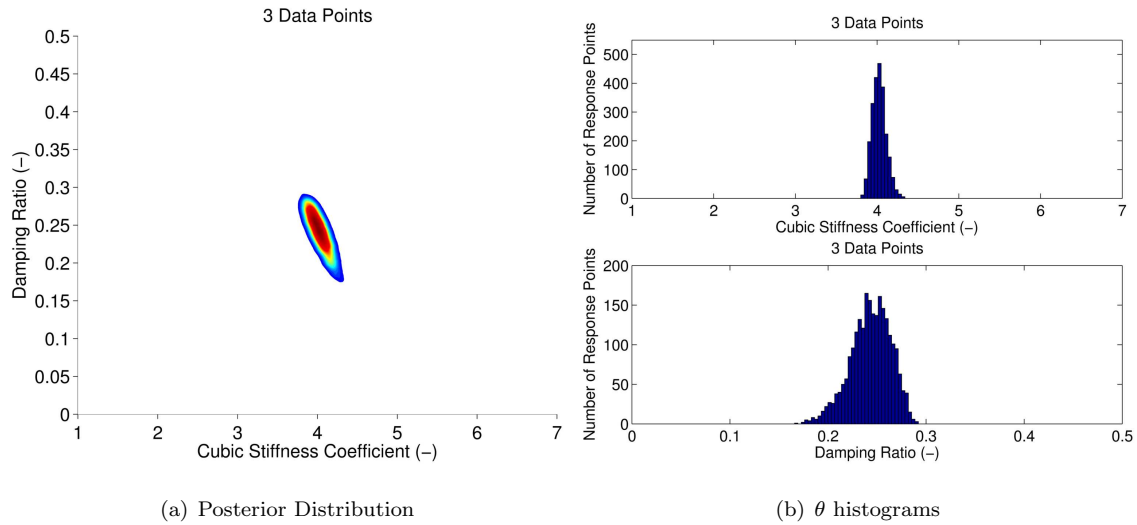

(a) Posterior Distribution

(b) θ histograms

Figure 4. Posterior and parameter distributions using data from 3 velocities - Aerofoil

Table 1. Convergence of Input Parameters - Aerofoil

No. of Data Points	Cubic Stiffness			Damping Ratio		
	Mean	% Error	Std dev.	Value	% Error	Std dev.
True	4	*N/A*	0	0.25	*N/A*	0
1	4.32364	8.091	0.55745	0.18442	26.232	0.10325
2	4.10302	2.576	0.25503	0.21935	12.260	0.07090
3	4.02121	0.530	0.10768	0.24369	2.524	0.02393
5	4.01671	0.418	0.09462	0.24506	1.976	0.02200

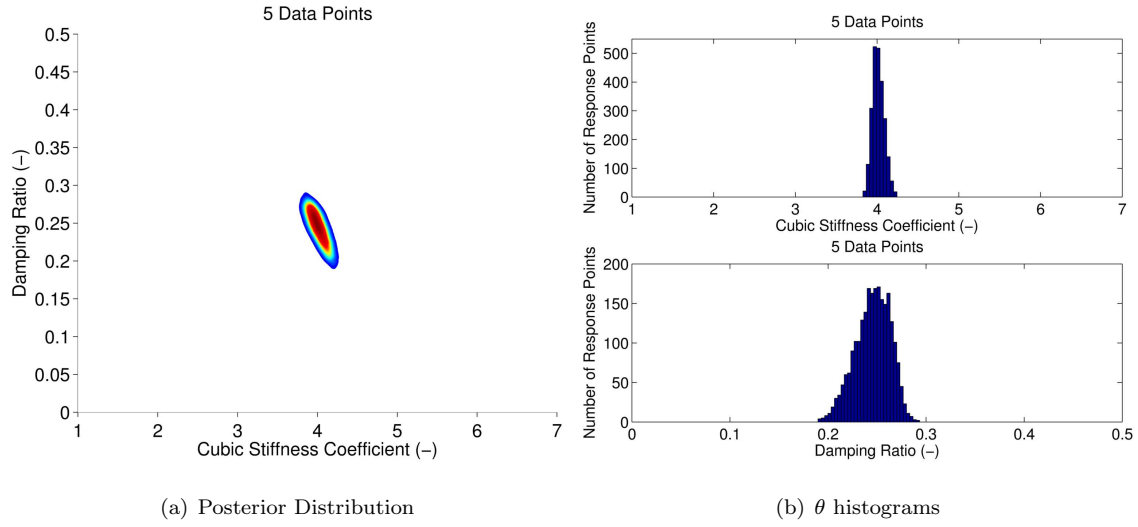(a) Posterior Distribution   (b) θ histograms

Figure 5. Posterior and parameter distributions using data from 5 velocities - Aerofoil
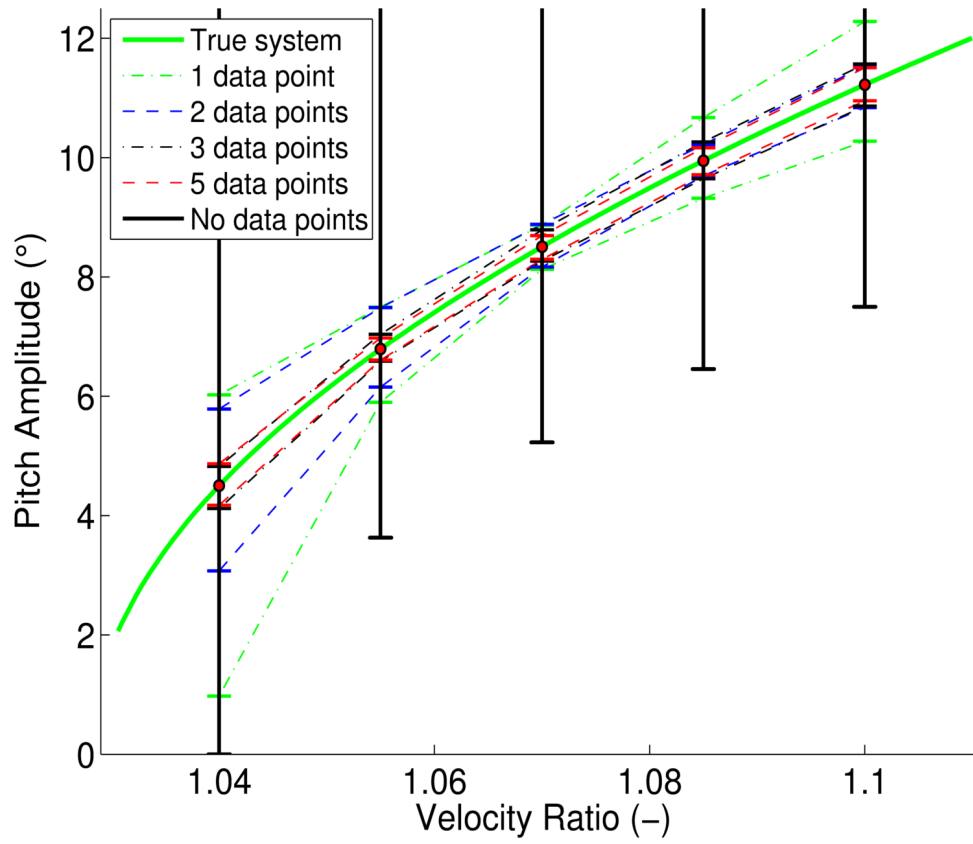

Figure 6. Uncertainty bars of aerofoil for variability across posterior distributions

The selection of the parameter values from the posterior distribution can present a problem because deterministic values are being inferred from a continuous distribution. This can have an impact on model performance. Thus the process of parameter selection from the posterior distributions is open to debate; mean, median and modal approaches could all be justified. However, the true values can be said to be contained within the posterior distribution with certainty, providing the evidence is valid. So if the model performs well for all parameter values within the posterior region, the Bayesian inference has been a success. Figure 6 shows the variability in LCO amplitude based on all combinations of parameter values within each posterior distribution. The error bars shown represent the worst case error which the model can have when the parameters are chosen from the posterior. The baseline case (no data points) is the variability from the entire parameter space as shown in Figure 1. Supporting previous observations, the performance of the model improves with increasing amounts of evidence. The model performance is improved the most close to the velocities which are considered in the MCMC. Therefore to ensure the best global model performance, it is important that the experimental data covers a wide range of velocities. Looking at the potential error in the model when only one experimental point is considered, it is clear that the error is smaller at the velocity which corresponds to the data. Likewise for two experimental data points the model performance is much better at higher velocities where the calibration takes place. Using three data points gives a globally small error as the velocities that were considered span the entire range of the velocities of interest. The performance of the MCMC using 5 data points gives a worst case variability of 7.3%. It is worth mentioning that all of the standard selection criteria mentioned above would produce a model that has significantly less error than the worst case.

Table 2 shows the time taken and the rejection rate of the MCMC for varying number of experimental data points. The inclusion of more evidence increases the cost of the MCMC in two ways: the number of simulations per MCMC sample is proportional to the number of data points, the increased number of data points yield an increased rejection rate of the MCMC. Subsequently, more model evaluations are required.

Table 2. Cost of MCMC - Aerofoil

No. of Data Points	Time (s)	Rejection Rate (%)
1	310	50.1
2	955	63.8
3	1556	68.2
5	3100	74.0

V.   Goland Wing

The Goland wing provides a relatively simple 3D model exhibiting several complex aeroelastic phenomenon that are challenging to engineering prediction methods. The wing has a rectangular plan-form with a span of $20 ft$ and $6 ft$ chord. The finite element model of the heavy version of the Goland wing is described in[20] and is shown in Figure 7(a). The structural model used in this work includes localised nonlinearities between the tip store attachment stiffness and the wing. The nonlinearities are in the form of polynomial laws for spring elements in the translational z-direction, K_z and the rotational y-direction, K_{ry} degrees of freedom which were shown to be the most sensitive by reference.[21] The equations of motion for the Goland wing take the same form as eq. (1). The external forces, $\mathbf{F}$ acting on the wing are aerodynamic in nature. NASTRAN computes these forces in the modal domain using Doublet-Lattice method. Thus the wing is analysed in the modal domain, this also significantly reduces the complexity of the problem.[22] The transformation between the physical and modal space[23] is given as $\{x\} = [\mathbf{\Phi}] \{\mathbf{q}\}$, where $\mathbf{\Phi}$ is the truncated matrix of eigenvectors, (n_m modes, extracted from NASTRAN) and $\mathbf{q}$ is a vector of n_m modal coordinates.

The aerodynamic data is only computed for a range of discrete reduced frequencies so it is represented as a rational function to maintain validity for all values within this range.[24] For this investigation only four structural modes are considered and are shown in Figure 7(b). The system in the modal domain with modal
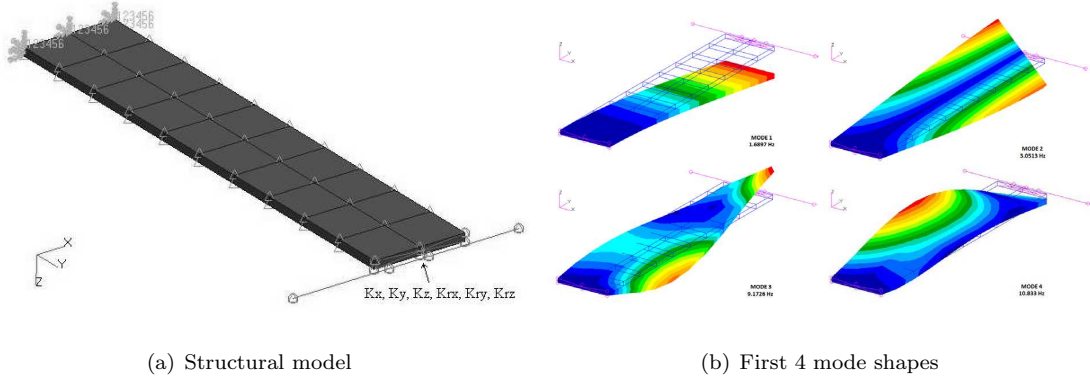
(a) Structural model   (b) First 4 mode shapes

Figure 7. Goland wing

coordinates, $\mathbf{q}$ is given as:[21, 25]

$$\tilde{\mathbf{M}}_\phi \ddot{\mathbf{q}} + \tilde{\mathbf{C}}_\phi \dot{\mathbf{q}} + \tilde{\mathbf{K}}_\phi \mathbf{q} + \mathbf{K}_{nl}(\mathbf{q}) = \frac{\rho V^2}{2} \sum_{i=1}^{n_l} [\mathbf{A}_{i+2}] \, \dot{\mathbf{q}}_{a_i} \tag{21}$$

where $\tilde{\mathbf{M}}_\phi$, $\tilde{\mathbf{C}}_\phi$, $\tilde{\mathbf{K}}_\phi$ and $\mathbf{K}_{nl}(\mathbf{q})$ are the aeroelastic system mass, damping, linear and nonlinear stiffness matrices respectively.[9] $\mathbf{A}_\bullet$ represents the rationally approximated components of the generalised aerodynamic matrix extracted from NASTRAN. $\dot{\mathbf{q}}_{a_i}$ are augmented terms arising from the Laplace domain treatment of the generalised aerodynamic matrix and have the relationship:

$$\ddot{\mathbf{q}}_{a_i} = \dot{\mathbf{q}} - \frac{V}{b} \eta_i \dot{\mathbf{q}}_{a_i} \tag{22}$$

Equations (21) and (22) can be combined and displayed in state space format:

$$\dot{\mathbf{w}} + \mathbf{A_s}\mathbf{w} + \mathbf{u} = 0 = \mathbf{R} \tag{23}$$

where

$$\mathbf{w} = \left\{ \begin{array}{c} \mathbf{q} \\ \dot{\mathbf{q}} \\ -\mathbf{A}_3\dot{\mathbf{q}}_{a_1} \\ -\mathbf{A}_4\dot{\mathbf{q}}_{a_2} \\ \vdots \\ -\mathbf{A}_{n_l+2}\dot{\mathbf{q}}_{a_{n_l}} \end{array} \right\}, \quad \mathbf{u} = \left\{ \begin{array}{c} \mathbf{0} \\ \tilde{\mathbf{M}}_\phi^{-1}\boldsymbol{\Phi}^{\mathrm{T}}\mathbf{K}_{nl}(\mathbf{q}) \\ \mathbf{0} \\ \mathbf{0} \\ \vdots \\ \mathbf{0} \end{array} \right\}$$

and

$$\mathbf{A}_s = \begin{bmatrix} \mathbf{0} & -\mathbf{I} & \mathbf{0} & \cdots & \cdots & \mathbf{0} \\ \tilde{\mathbf{M}}_\phi^{-1}\tilde{\mathbf{K}}_\phi & \tilde{\mathbf{M}}_\phi^{-1}\tilde{\mathbf{C}}_\phi & \tilde{\mathbf{M}}_\phi^{-1}\frac{\rho V^2}{2}\mathbf{I} & \cdots & \cdots & \tilde{\mathbf{M}}_\phi^{-1}\frac{\rho V^2}{2}\mathbf{I} \\ \mathbf{0} & \mathbf{A}_3 & \frac{V}{b}\eta_1\mathbf{I} & \mathbf{0} & \cdots & \mathbf{0} \\ \mathbf{0} & \mathbf{A}_4 & \mathbf{0} & \frac{V}{b}\eta_2\mathbf{I} & \ddots & \vdots \\ \vdots & \vdots & \vdots & \ddots & \ddots & \mathbf{0} \\ \mathbf{0} & \mathbf{A}_{n_l+2} & \mathbf{0} & \cdots & \mathbf{0} & \frac{V}{b}\eta_{n_l}\mathbf{I} \end{bmatrix}$$

Applying the HDHB method to eq. (21) yields the system:

$$\left[\tilde{\mathbf{M}}_\phi \mathbf{E}_{acc}^{-1} + \tilde{\mathbf{C}}_\phi \mathbf{E}_{vel}^{-1} + \tilde{\mathbf{K}}_\phi \mathbf{E}_{def}^{-1} \right] \hat{\mathbf{Q}}_\phi + \mathbf{E}_{def}^{-1}\hat{\mathbf{K}}_{nl} - \frac{\rho V^2}{2} \sum_{i=1}^{n_l} [\mathbf{A}_{i+2}] \, \mathbf{E}_{def}^{-1}\hat{\mathbf{Q}}_{a_i} = 0 \tag{24}$$

$\mathbf{E}_{acc}^{-1}$, $\mathbf{E}_{vel}^{-1}$ and $\mathbf{E}_{def}^{-1}$ are transformation matrices shown in.[9] The complexity of both the nonlinear stiffness force, $\{\hat{\mathbf{K}}_{nl}\}$ and the decomposed generalised aerodynamic vectors, $\{\hat{\mathbf{Q}}_{a_i}\}$ prevent the straightforward representation of these terms in the frequency domain. Subsequently system (24) is a time domain representation

of the problem, where the nonlinear terms are represented as reconstructed Fourier series. The Fourier coefficients are formed using discrete Fourier transforms (DFT) and are computed numerically as described in.[9] Equation (24) is solved simultaneously for $2N_H + 1$ equally spaced time steps across one period with $t_i = \frac{i2\pi}{2n_H+1}$, $(i = 0, 1, ..., 2N_H)$ to maintain temporal accuracy. A Newton-Raphson scheme is employed and as in the previous case; the response frequency is maintained as a variable by locking the *cosine* Fourier coefficient of the first harmonic of the first mode to zero.

Results

For the Goland wing, structural variability is imposed at the FE analysis stage to generate new mode-shapes and modal frequencies for the aeroelastic simulation. The NASTRAN analysis provides the behaviour of the wing for linear stiffness only. Hence the nonlinear stiffness and damping behaviour of the wing is hard-wired. The cubic stiffness coefficients in the z (K_z), and rotational y (K_{ry}) degrees of freedom were given values of $10^{10.95}$ and 10^{10} respectively. There is no nonlinear component of damping in this work but the linear damping matrix, $\tilde{\mathbf{C}}_\phi$ is given a damping coefficient of 0.1. In reference[9] eight structural parameters were investigated, in this work the two most sensitive parameters were identified and selected to be the uncertain parameters: the trailing edge spar thickness and the store centre of gravity (CG) chord-wise location which were given *true* values of $0.0006ft$ and $0ft$ respectively. Due of the large number of simulation evaluations which are needed for MCMC, the cost of running the HDHB would be excessive. To mitigate this, an artificial neural network (ANN) is trained using 5000 Latin hyper-cube samples from the selected parameter space. Evaluation of the ANN for a given set of inputs is very cheap in comparison to the HDHB simulations and many more MCMC samples are attainable, thus in this case, 40000 MCMC samples are employed with a burn-in of 5000 samples. The training of the ANN took $27630s$ and testing found the ANN to be within 2% accuracy of the HDHB which is deemed acceptable. The experimental data in this case is a series of simulations performed at different velocities using the time-domain solver employed in reference.[9] The time domain simulations took approximately $160s$ each whereas the HDHB took $17s$ per sample hence it is much more suitable for training the ANN. The HDHB samples were computed using 1 harmonic and the majority of the time taken for a sample is spent on the FE analysis to create the new modeshapes and frequencies as only the LCO prediction phase of each sample is sped up.
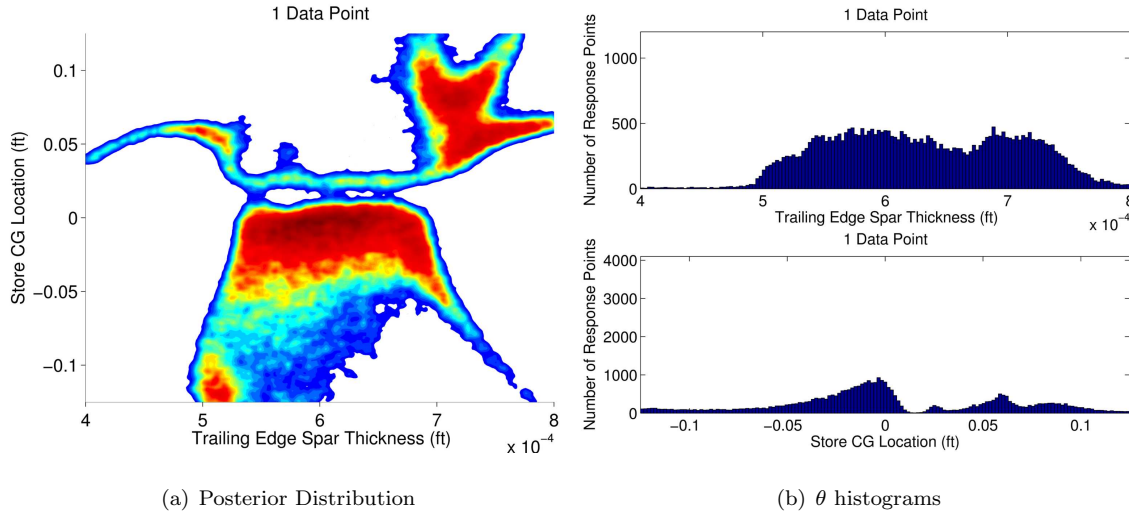

(a) Posterior Distribution

(b) θ histograms

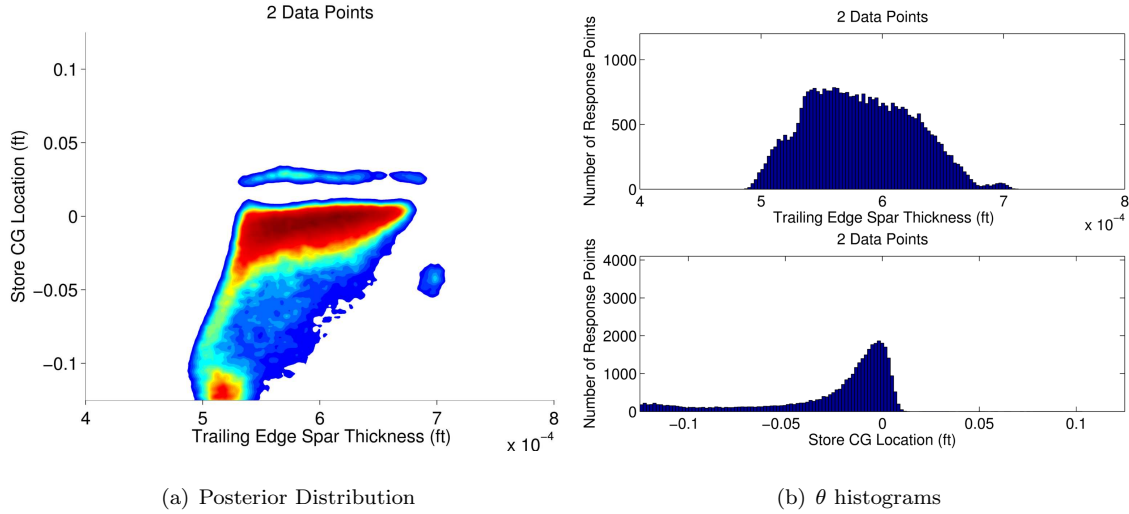**Figure 8. Posterior and parameter distributions using data from 1 velocity - Goland Wing**

The posterior distribution and histograms for 1 data point ($715fts^{-1}$) are shown in Figure 8 where the store CG location represents a translation in the chord-wise direction from the nominal position of $0.25ft$ downstream of the leading edge, positive translation denotes movement towards the trailing edge. Immediately it is evident that the posterior takes a radical form, much more complex than in the aerofoil case. This is caused by the indirect interaction between fundamental structural parameters and the LCO prediction. The store CG location in particular has a highly nonlinear relationship with stability due to a significant change in the modeshapes of the structure; changing the modeshapes alters the way the structure

interacts with the flow and this is the source of the peculiar posterior shape. Evidence of the modeshape variability induced by changes in these structural parameters can be found in.[26] It is possible to see an underlying trend amongst the distinctive shape of the posterior; most of the regions of high probability show a positive correlation between the two parameters. As the store CG location increases, stability will decrease thus spar thickness also needs to increase to compensate for the change in stability.

The distributions and histograms for 2, 3 and 5 points are shown in Figures 9, 10 and 11. The velocities considered for each case are shown in Table 3. It is evident from the posterior plots that the distribution is reduced in size when more points are considered, as in the aerofoil case. When the low velocity of $700 fts^{-1}$ is introduced, the regions of high store CG location are removed as the model fails to coincide with the time domain solution at this velocity. Further refinement from adding more velocities restricts the posterior to a narrow range of store location and quite a wide range of spar thickness. As a result it is concluded that the store location is the more important factor for model performance and this is concurrent with results shown in.[26]

Table 3. Goland Wing Velocities

No. of Data Points	Velocities (fts^{-1})
1	715
2	700, 715
3	700, 715, 730
5	700, 710, 715, 720, 730

(a) Posterior Distribution

(b) θ histograms

Figure 9. Posterior and parameter distributions using data from 2 velocities - Goland Wing

Inspection of the histograms in Figures 9(b), 10(b) and 11(b) illustrate the reduction of the store CG location variability with increased data points. The distributions develop into a well-formed skewed Gaussian distribution with the modal value at the true value and minimal samples above the true value. This is due to the decrease in stability which occurs when the store location is moved towards the trailing edge; as stability decreases, the LCO amplitude becomes more sensitive to variability thus the model will start to fail much closer to the true value than when the store is moving towards the leading edge. There is a small refinement of the trailing edge spar thickness distribution when the number of data points is increased as it is the less influential parameter. There is a noticeable change occurring in the spar thickness distribution shape from one case to the next. This is believed to be caused by the low impact this parameter has on the acceptance of a sample at these conditions. Consequently, 40000 MCMC samples is inadequate for achieving a statistically converged distribution for this parameter. Nevertheless, the ability to estimate the true parameter value has not been comprised as shown in Table 4 where the mean values of the distributions move closer towards the true values and standard deviation decreases. The mean value for store CG location for 1 data point
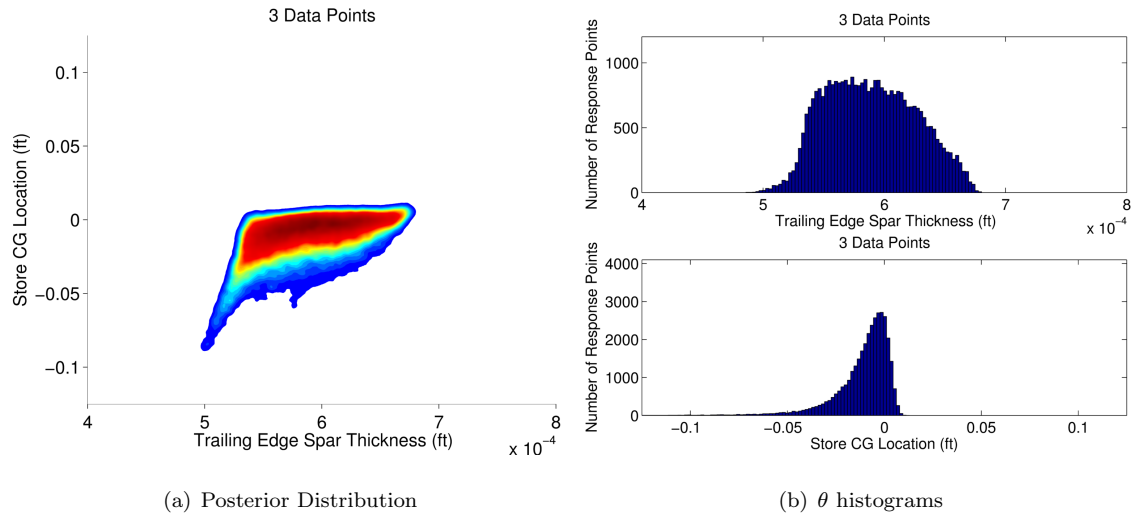
(a) Posterior Distribution

(b) θ histograms

Figure 10. Posterior and parameter distributions using data from 3 velocities - Goland Wing

(a) Posterior Distribution
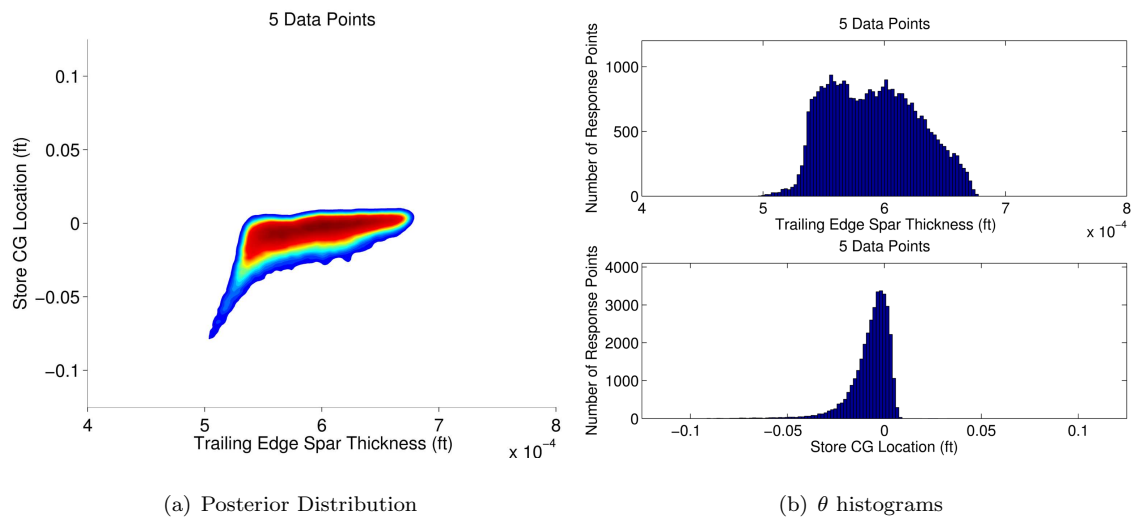
(b) θ histograms

Figure 11. Posterior and parameter distributions using data from 5 velocities - Goland Wing

is in fact the closest to the true value of $0 ft$ but this is not considered to be meaningful because of the radical shape of the distribution. It is worth mentioning that the percentage error for the store CG location is normalised using the width of its prior, ie. $0.25 ft$.

Table 4. Mean Values of Input Parameters - Goland Wing

No. of Data Points	TE Spar Thickness			Store CG Location		
	Mean ($\times 10^{-4}$)	% Error	Std dev. ($\times 10^{-5}$)	Mean	% Error	Std dev.
True	6.0000	*N/A*	0	0	*N/A*	0
1	6.3132	5.220	7.4859	0.0014	0.560	0.0550
2	5.8196	3.007	4.2980	-0.0234	9.360	0.0345
3	5.8879	1.868	3.6827	-0.0111	4.440	0.0152
5	5.9120	1.467	3.6275	-0.0070	2.800	0.0102

The computational times for each case are shown in Table 5. The times are comparable with that of the aerofoil case however there is almost twice as many samples in the Goland wing highlighting the benefit of the ANN. The rejection rates are lower than that of the aerofoil case which performed very well, this is caused by the size of the proposal distribution. This influences how much the parameters change from one MCMC sample to the next. For optimum performance, the proposal distribution should be similar in size and shape of the posterior distribution which is not known *a priori*. Here the proposal distribution is slightly smaller than the posterior which leads to an increased acceptance rate allowing the required amount of MCMC samples to be reached sooner. However this has the disadvantage of requiring more MCMC samples to fully cover the posterior distribution and thus needing more MCMC samples to reach statistical convergence which accounts for the lack of statistical convergence in the Goland wing case.

Table 5. Cost of MCMC - Goland Wing

No. of Data Points	Time (s)	Rejection Rate (%)
1	724	37.4
2	1393	39.9
3	2053	40.7
5	3984	51.4

VI.   Conclusions

Estimation of various structural parameters was conducted for a pitch/plunge aerofoil and Goland wing configuration based on limit cycle oscillation behaviour. A Bayesian inference methodology with Markov-chain Monte Carlo (MCMC) was employed which utilised *experimental* data to reduce the parameter distributions. The experimental data was simulated using the model for the aerofoil case and a time marching code was used to generate the Goland wing data. The efficiency of the high-dimensional harmonic balance was exploited to cheaply drive the MCMC in the aerofoil case. For the Goland wing the harmonic balance was used to train an artificial neural network which was used for the MCMC. In both cases it was evident that the addition of more external data refined the posterior distribution and enabled the estimation of the *true* parameter values to be progressively more accurate. Observation of the shape of the posterior is necessary to correctly quantify the reduction in variability which has been achieved. The Bayesian framework also gave insights to how the different parameters influenced the limit cycle oscillation amplitude. The importance of the proposal distribution size and shape was discussed. The Bayesian inference performed well and was shown to be practical for these types of problems.

VII.   Acknowledgements

References

[1] C. Pettit, Uncertainty Quantification in Aeroelasticity: Recent Results and Research Challenges, Journal of Aircraft 41 (5) (2004) 1217–1229.

[2] S. Marques, K. Badcock, H. Khodaparast, J. Mottershead, Transonic Aeroelastic Stability Predictions Under the Influence of Structural Variability, Journal of Aircraft 47 (4) (2010) 1229–1239.

[3] S. Marques, K. Badcock, H. Khodaparast, J. Mottershead, How Structural Model Variability Influences Transonic Aeroelastic Stability, Journal of Aircraft 49 (5) (2012) 1189–1199, doi:10.2514/1.C031103.

[4] R. Bunton, C. Denegri, Limit Cycle Oscillation Characteristics of Fighter Aircraft, Journal of Aircraft 37 (5) (2000) 916–918.

[5] J. Thomas, E. Dowell, K. Hall, C. Denegri, Modeling Limit Cycle Oscillation Behavior of the F-16 Fighter Using a Harmonic Balance Approach (AIAA-2004-1696), presented at the 45th AIAA/ASME/ASCE/AHS/ASC Structures, Structural Dynamics, and Materials Conference, Palm Springs, California.

[6] P. Beran, C. Pettit, D. Millman, Uncertainty Quantification of Limit-Cycle Oscillations, Journal of Computational Physics 217 (1) (2006) 217–247.

[7] J. Witteveen, A. Loeven, S. Sarkar, H. Bijl, Probabilistic collocation for period-1 limit cycle oscillations, Journal of Sound and Vibration 311 (12) (2008) 421–439, doi:10.1016/j.jsv.2007.09.017.

[8] J. L. Meitour, D. Lucor, C. Chassaing, Prediction of stochastic limit cycle oscillations using an adaptive Polynomial Chaos method, Journal of Aeroelasticity and Structural Dynamics 2 (1) (2010) 3–22.

[9] R. Hayes, S. Marques, Prediction of limit cycle oscillations under uncertainty using a Harmonic Balance method, Computers and Structures 148 (2015) 1–13.

[10] M. Kennedy, A. O'Hagan, Bayesian calibration of computer models, Journal of the Royal Statistical Society B 63 (3) (2001) 425–464.

[11] R. Dwight, H. Haddad-Khodaparast, J. Mottershead, Identifying structural variability using Bayesian inferenceIn proceedings of International Conference on Uncertainty in Structural Dynamics (ISMA/USD), Leuven, Belgium.

[12] W. Edeling, P. Cinnella, R. Dwight, H. Bijl, Bayesian estimates of parameter variability in the k-ϵ turbulence model, Journal of Computational Physics 258 (2014) 73–94.

[13] R. Dwight, H. Bijl, S. Marques, K. Badcock, Reducing Uncertainty in Aeroelastic Flutter Boundaries using Experimental Data (IFASD-2011-71), presented at the International Forum for Aeroelasticity and Structural Dynamics, Paris, France.

[14] K. Hall, J. Thomas, W. Clark, Computation of Unsteady Nonlinear Flows in Cascades Using a Harmonic Balance Technique, AIAA Journal 40 (5) (2002) 879–886.

[15] L. Liu, J. Thomas, E. Dowell, P. Attar, K. Hall, A comparison of classical and high dimensional harmonic balance approaches for a Duffing oscillator, Journal of Computational Physics 215 (1) (2006) 298–320, doi:10.1016/j.jcp.2005.10.026.

[16] J. Thomas, E. Dowell, K. Hall, Nonlinear Inviscid Aerodynamic Effects on Transonic Divergence, Flutter, and Limit-Cycle Oscillations, AIAA Journal 40 (4) (2002) 638–646.

[17] W. Hastings, Monte Carlo Sampling Methods Using Markov Chains and Their Applications, Biometrika 57 (1) (1970) 97–109.

[18] B. Lee, L. Liu, K. Chung, Airfoil motion in subsonic flow with strong cubic nonlinear restoring forces, Journal of Sound and Vibration 218 (35) (2005) 699–717, doi:10.1016/j.jsv.2004.01.034.

[19] B. Lee, L. Gong, Y. Wong, Analysis and Computation of Nonlinear Dynamic Response of a two-Degree-of-Freedom System and its Applications in Aeroelasticity, Journal of Fluids and Structures 11 (FL960075) (1997) 225–246.

[20] P. Beran, N. Knot, F. Eastep, R. Synder, J. Zweber, Numerical Analysis of Store-Induced Limit Cycle Oscillation, Journal of Aircraft 41 (6) (2004) 1315–1326.

[21] K. Badcock, H. Khodaparast, S. Timme, J. Mottershead, Calculating the Influence of Structural Uncertainty on Aeroelastic Limit Cycle Response (AIAA-2011-1741), presented at the 52nd AIAA/ASME/ASCE/AHS/ASC Structures, Structural Dynamics, and Materials Conference, Denver, Colorado.

[22] M. Platten, J. Wright, K. Worden, G. Dimitriadis, J. Cooper, Non-linear identification in modal space using a genetic algorithm approach for model selection, International Journal of Applied Mathematics and Mechanics 3 (1) (2007) 72–89.

[23] M. Platten, J. Wright, G. Dimitriadis, J. Cooper, Identification of multi-degree of freedom non-linear systems using an extended modal space approach, Journal of Mechanical Systems and Signal Processing 23 (2009) 8–29.

[24] W. Eversman, A. Tewari, Consistent Rational-Function Approximation for Unsteady Aerodynamics, Journal of Aircraft 28 (9) (1991) 545–552.

[25] G. Dimitriadis, G. Vio, J. Cooper, Application of Higher-Order Harmonic Balance to Non-Linear Aeroelastic Systems (AIAA-2006-2023), presented at the 47th AIAA/ASME/ASCE/AHS/ASC Structures, Structural Dynamics, and Materials Conference, Newport, Rhode Island.

[26] R. Hayes, S. Marques, W. Yao, The influence of Structural Modeshape Variability on Limit Cycle Oscillation Behaviour-Paper presented at 15th AIAA/ISSMO Multidisciplinary Analysis and Optimization Conference, Atlanta, Georgia.